Volume 3
Number 1
January 2026
Pages 1–202

RSC Applied Interfaces

rsc.li/RSCApplInter

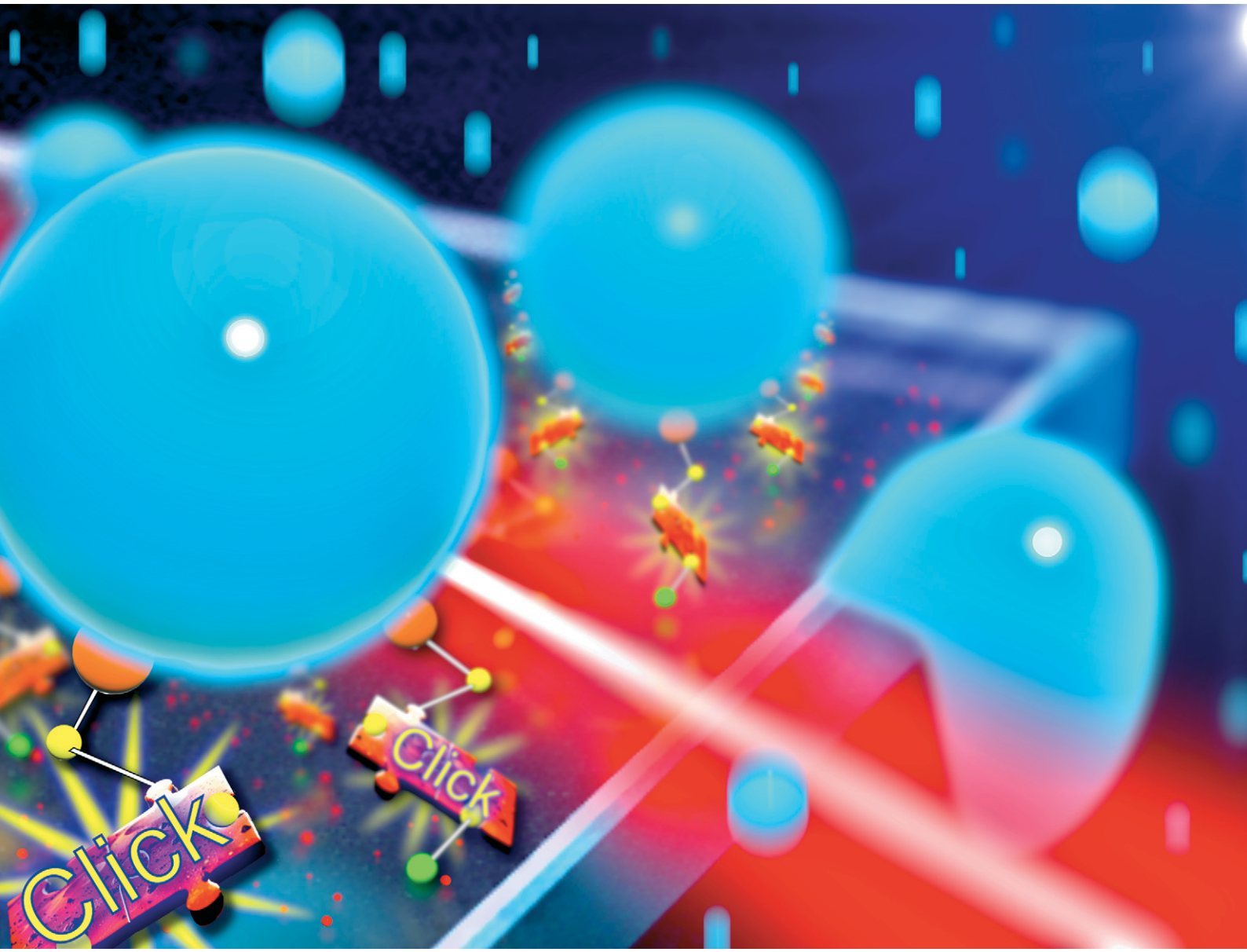

ISSN 2755-3701

ROYAL SOCIETY OF CHEMISTRY

PAPER
Mohamed Siaj, Ali Nazemi *et al.*
From vinyl to allyl: how a single-carbon difference alters glass surface architecture, reactivity and function

RSC Applied Interfaces

ROYAL SOCIETY OF CHEMISTRY

PAPER

View Article Online
View Journal | View Issue

Check for updates

Cite this: *RSC Appl. Interfaces*, 2026, 3, 45

From vinyl to allyl: how a single-carbon difference alters glass surface architecture, reactivity and function

Nesrine Khitas,[a] Maziar Jafari,[a] Calvin C. H. Cheng,[b] Mohamed Siaj *[a] and Ali Nazemi *[a]

Natural non-wettable surfaces, such as lotus leaves, exhibit exceptional self-cleaning properties due to their unique micro- and nanostructures. This has inspired researchers to develop artificial superhydrophobic materials, particularly on mica and SiO_2-based substrates, such as glass, using organosilanes to achieve tailored properties. This study focused on modifying glass surfaces with vinyltrichlorosilane (VTCS) and allyltrichlorosilane (ATCS) to create coatings with enhanced optical properties, wettability, and stability. We employed a two-step surface modification strategy: dip-coating followed by functionalization with 1-decanethiol through radical-initiated thiol–ene click reaction to functionalize these surfaces with a long alkyl chain to enhance hydrophobicity and improve chemical stability. The morphology, structure, and chemical composition of the coatings were characterized by using a combination of techniques, including scanning electron microscopy, atomic force microscopy, attenuated total reflectance-Fourier transform infrared spectroscopy, and photo-induced force microscopy (PiFM). PiFM was specifically employed to assess the uniformity of surface functionalization, both at the surface and throughout the film's depth, and to quantify the efficiency of the thiol–ene click reaction.

Received 4th June 2025,
Accepted 1st September 2025

DOI: 10.1039/d5lf00162e

rsc.li/RSCApplInter

Open Access Article. Published on 02 September 2025. Downloaded on 2/12/2026 8:12:20 PM.
This article is licensed under a Creative Commons Attribution 3.0 Unported Licence.

Introduction

The remarkable self-cleaning properties of some plant surfaces,[1,2] especially the lotus leaf,[1,3] have attracted the attention of researchers and have inspired the development of artificial hydrophobic and superhydrophobic surfaces.[4–11] These natural surfaces combine micro- and nanostructures with a waxy coating, resulting in high water contact angles and low sliding angles.[1,12] The unique combination of surface topography and surface chemistry is responsible for water repellency and self-cleaning properties,[13] making them ideal models for replication.[14] In parallel, surface modification of inorganic materials using organosilanes has emerged as a practical approach to achieve tailored surface properties that mimic the natural non-wettable surfaces.[15] While this modification technique applies to various oxide surfaces,[16] the most studied systems include alkyl trichlorosilanes on SiO_2-based substrates,[17] including silicon wafer,[18] glass,[19–21] and mica.[22–25]

The reactivity of the trichlorosilane precursors is highly dependent on the choice of their chemical composition, functional groups, reaction conditions, and substrate properties. Under proper conditions, the silane precursors will self-assemble into monolayers through horizontal polymerization. Subsequently, they react with existing surface silanols, resulting in the formation of covalently bonded monolayers. Additionally, silane precursors have demonstrated a capacity to condense with water and surface silanols, leading to the formation of covalently attached, crosslinked polymeric layers through vertical polymerization.[15] Early investigations in this field predominantly focused on silanes and siloxanes with relatively simple molecular structures, where silicon atoms were primarily bound to short[21,26,27] or long-chain alkyl groups.[28–32] These nonreactive functional groups are often challenging to functionalize and may require harsh conditions.[33–35] However, current trends in chemistry have shifted towards silanes with functionalizable groups such as amines, thiols as well as alkenes.[36] This shift has opened up new possibilities for tailoring material properties under mild conditions, expanding their potential applications across diverse technological sectors[37] such as optoelectronics,[38,39] microfluidics,[40] and biosensing.[9,41] While vinyl- and allyltrichlorosilanes have demonstrated utility in organic synthesis,[42] their application to glass surface modification remains less studied[43,44] compared to other organosilanes[45] such as alkyl- and perfluoroalkyltrichlorosilanes including

[a] *Department of Chemistry, Université du Québec À Montréal, Montréal, H3C 3P8, QC, Canada. E-mail: siaj.mohamed@uqam.ca, nazemi.ali@uqam.ca*
[b] *Edgehog Advanced Technologies Inc., Montréal, H3C 2G9, QC, Canada*

© 2026 The Author(s). Published by the Royal Society of Chemistry

Open Access Article. Published on 02 September 2025. Downloaded on 2/12/2026 8:12:20 PM. This article is licensed under a Creative Commons Attribution 3.0 Unported Licence.

alkoxysilanes.[21,27,29–32,46–50] These short-chain alkenylsilanes are of particular interest due to their reactive terminal C=C bond, enabling functionalization *via* thiol–ene click chemistry under mild conditions. The use of vinyl- and allyltrichlorosilanes started gaining attention in the mid-20th century.[51] These compounds were initially explored due to their ability to form covalent bonds with oxide surfaces, particularly glass.[52] Modification of oxide surfaces with organosilanes enabled various applications, including the improvement of adhesion of organic materials, the increase of the wear resistance of coatings and further chemical modifications.[53] In the 1940s and 1960s, researchers began investigating the use of these organosilanes as coupling agents for improving binding between inorganic materials and organic polymers. For instance, studies demonstrated the improved properties of polyester laminates treated with these silanes, showing significant strength improvements over their saturated derivatives (ethyl- and propyltrichlorosilanes).[51]

Early studies on allyltrichlorosilane (ATCS)-modified glass surfaces have shown their potential for subsequent functionalization. These modifications enable fine control over multifunctional surface properties such as inertness, wettability, and photoactivity, with applications ranging from gas chromatography capillaries[54] to nanotechnology.[55] The functionalization strategies offer complementary modifications, with one study increasing surface polarity through oxidation of the unsaturation in the allyl group, while another enhances hydrophobicity through a catalyst- and solvent-free 1,3-dipolar cycloaddition reaction, enhancing the surface's versatility for various applications.[54,55] Vinyltrichlorosilane (VTCS)-modified glass surfaces similarly allow for post-functionalization reactions through photoinduced disulfide–ene and thiol–ene click reactions.[43] Such approaches provide stable and tunable interfaces for biosensing and diagnostic applications while preserving the integrity of the silane layer. The developed VTCS-derived coatings achieved dual thiol/disulfide–ene reactivity, persistent superhydrophobicity, and direct protein conjugation.

Herein, we investigate glass surfaces modified by commercially available VTCS and ATCS *via* dip coating. We explore how a single-carbon variation in the used silanizing agent affects the resulting surface properties. We also investigate how functionalizing the surface with a long alkyl chain thiol through a thiol–ene click reaction enhances the stability of the superhydrophobic coatings. Our study includes in-depth surface analyses using a combination of attenuated total reflectance-Fourier transform infrared spectroscopy (ATR-FTIR), photo-induced force microscopy (PiFM), atomic force microscopy (AFM), scanning electron microscopy (SEM), water contact angle measurements, and UV-vis spectroscopy techniques. Notably, this study presents a novel application of PiFM to quantify the efficiency of the thiol–ene click reaction and to map the spatial distribution of functionalization both across the surface and throughout the depth of the films. These findings offer new insights into how subtle structural differences between silanizing agents can significantly influence surface properties.

Materials and methods

Materials

As substrates, soda-lime glass slides (27 mm × 46 mm × 1.2 mm thick) were supplied by Ward's Science (USA). Trichlorovinylsilane ($Cl_3SiCH{=}CH_2$, 97%) (VTCS), allyltrichlorosilane (Cl_3SiCH_2-$CH{=}CH_2$, 95%) (ATCS), 1-decanethiol (DSH) ($CH_3(CH_2)_9SH$, 96%), concentrated sulfuric acid (H_2SO_4, 98%) and hydrogen peroxide (H_2O_2, 30%) were purchased from Sigma-Aldrich and used without further purification. Benzene, toluene, ethanol, methanol, tetrahydrofurane were all reagent grade and used as received.

Glass silanization procedure. Firstly, the glass slides were cleaned using piranha solution (H_2SO_4 : H_2O_2), following the activation protocol of glass described in our previous study.[56] Then, the glass substrates were annealed at 200 °C for 1 h. Once cooled to room temperature, the activated glass samples were dip-coated in 8 mL of freshly prepared VTCS and ATCS solutions (40 mM) in benzene for 24 h. Under optimal humidity conditions (RH 40–60%), the reactions were carried out in closed vials with brief exposure to air during the introduction of the solutions and samples. When the ambient humidity is high (RH > 70%), the vials containing the activated glass samples were first purged with argon until cooled to room temperature before adding the solvent. The closed vials were only briefly exposed to air when adding silanizing agents. Finally, the vials were placed in a desiccator to maintain controlled humidity. The modified glass samples were rinsed with toluene, ethanol, and methanol, gently air-dried, and finally annealed for 10 min at 100 °C.

Surface post-modification reaction *via* thiol–ene click reaction. Glass surfaces with short-chain alkene-containing functionalities (*i.e.* vinyl and allyl) were investigated towards post-modification *via* thiol–ene click reaction using DSH to enhance the stability of the coatings. The silanized glass samples were immersed in a 20% (v/v) solution of DSH in tetrahydrofuran (THF), with ~0.05 eq. of azobisisobutyronitrile (AIBN) relative to the thiol. The reaction was conducted overnight under an inert atmosphere at 80 °C. The samples were then withdrawn from the solution, rinsed with hexane, ethanol, and methanol, gently air-dried, and finally annealed for 10 min at 100 °C. A schematic representation of the VTCS and ATCS coatings on the glass substrate followed by the thiol–ene click reaction is shown in Scheme 1. Notably, the dip-coating process enabled uniform functionalization across the entire glass substrate. For illustrative simplicity, the reactions of VTCS and ATCS with the glass substrate are depicted on a single surface. However, all optical characterizations account for modification on both sides, and any observed changes reflect functionalization across the entire substrate.

Characterization

An Attension Theta Optical Tensiometer (Biolin Scientific) was employed to study the wettability of the coated glass surfaces. Static water contact angles (θ) (WCAs) were measured at ambient temperature using 10 μL of deionized water. The

© 2026 The Author(s). Published by the Royal Society of Chemistry

Open Access Article. Published on 02 September 2025. Downloaded on 2/12/2026 8:12:20 PM.
This article is licensed under a Creative Commons Attribution 3.0 Unported Licence.

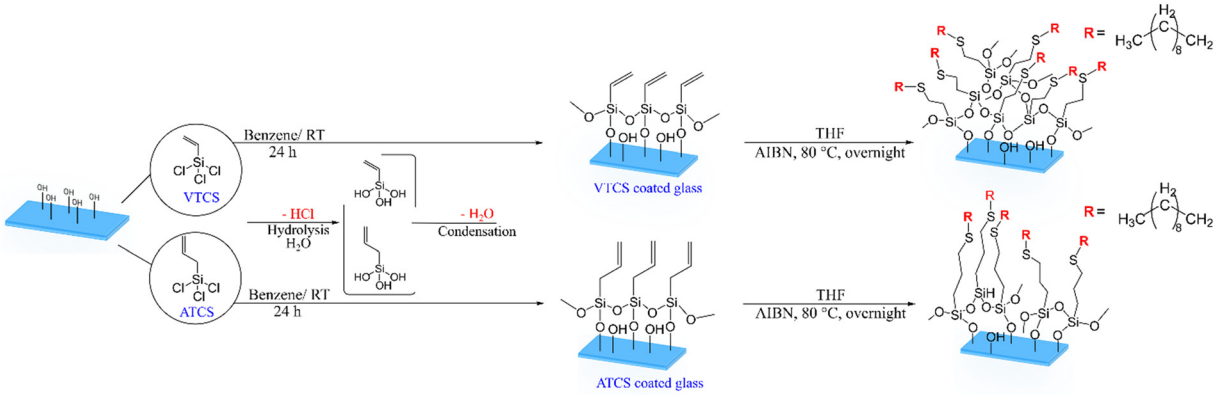

Scheme 1 The reactions of VTCS and ATCS on glass substrate followed by thiol–ene click reaction.

reported values represent the average of three measurements taken at random positions on each sample. Sliding angles of the control samples were measured using the same instrument with 10 μL droplets. A Lambda 750 UV/vis/NIR spectrophotometer (PerkinElmer, USA) was used to study the transmittance and reflectance of the coatings. A Nicolet iS50 Fourier transformed infrared spectrometer (Thermo Scientific, USA) was used to confirm the fixation of the silanization agents on the glass surface and the functionalization of alkenes. Surface topography and roughness were analyzed using a multimode 8 (Bruker, USA) atomic force microscope (AFM). A JEOL JSM-7600F scanning electron microscope (SEM) (Japan) was used to examine the morphology of the coatings. Chemical identities, topography, and quantification of the surface coverage were determined using a photo-induced force microscope (PiFM) on a VistaScope instrument (Molecular Vista, Inc., USA). PiFM spectra and images result from deconvoluting a summed heterodyne signal ($f_1 + f_2$). This signal is observed by lock-in amplifiers tracking two different cantilever resonant modes, termed f_1 and f_2, where $f_1 < f_2$. The f_2 frequency is exclusive to topographic imaging. PiFM imaging is slightly more complex, as there are two principal origins which depend on the pulsing frequency (f_m) of the source irradiation. The more straightforward method, also termed direct mode, is to pulse the IR laser at the cantilever frequency (f_1). Direct mode enables laser penetration deep into the sample, triggering a stronger photothermal expansion effect which is sensed by the tip. This mode is ideal for bulk surface characterization with nanometer lateral spatial resolution. The sideband mode is the image resulting from the laser pulsing at the differential frequency $f_m = f_2 - f_1$. The laser pulsing at midpoint between the two cantilever modes has been proven to yield surface-sensitive (~10–20 nm depth) spectroscopy and chemical imaging, generated by the contributions of sample molecule induced-dipoles and photothermal expansion.[57]

Results and discussion

The glass surfaces were coated with VTCS and ATCS, short-chain alkenylsilanes chosen for their reactive terminal double bonds, which allow further surface modification. The coating process involved the hydrolysis and condensation of VTCS and ATCS, forming covalent siloxane bonds with the glass surface while preserving the alkene functionality. FTIR spectroscopy was carried out to confirm the covalent bonding of VTCS and ATCS coatings on the glass surfaces. These short alkenylsilanes were interesting because their unsaturated bond functionality allows further surface modification.[43,58,59] The transmittance ATR-FTIR spectra of pristine glass, VTCS- and ATCS-modified glass samples were recorded in the 4000–650 cm^{-1} range. Due to the strong absorption of the glass substrate at wavenumbers below 1200 cm^{-1}, which can be seen as the broad peak in the transmittance spectrum (Fig. S1), an entire spectral range was not represented. Consequently, it is inconvenient to determine the presence of any peaks below 1200 cm^{-1} in the spectra that could be associated with the VTCS or ATCS coatings. Therefore, peaks associated with the silicon head group, Si–CH_2, Si–O–Si or Si–C overlap with the absorption of the glass substrate and are not observed in the lower frequency ranges of these spectra.

VTCS and ATCS fixation on glass surfaces

To the best of our knowledge, the only infrared spectroscopy study of VTCS-coated glass was previously reported by R. Harrop,[60] revealing key features at 1639 cm^{-1}, 1450 cm^{-1}, and 971 cm^{-1}, corresponding to C=C stretching, –CH_2 in-plane bending, and –CH_2 out-of-plane bending modes, respectively. However, this study does not discuss the full mid-infrared region (4000–400 cm^{-1}), particularly the C–H stretching region (3100–2800 cm^{-1}), which is crucial for a more comprehensive analysis of the organosilane coating. This research gap highlights the need for a more complete spectral analysis to fully characterize the VTCS coating on glass surface. Later on, Shen and co-workers[61] conducted a detailed vibrational analysis of VTCS using infrared and Raman spectroscopy, supported by computational calculations (*ab initio*). While their studies focused only on the pristine forms of VTCS (gaseous, solid, liquid, and

Open Access Article. Published on 02 September 2025. Downloaded on 2/12/2026 8:12:20 PM.
This article is licensed under a Creative Commons Attribution 3.0 Unported Licence.

dissolved in liquid xenon), their findings provide valuable insights into the vibrational behavior of VTCS, which may contribute to a better understanding of the vibrational behavior of VTCS on glass.

In the current study, we have successfully assigned the VTCS and ATCS characteristic vibrational frequencies (Fig. 1). Considering the spectral regions 3150–2800 cm^{-1} (top) and 1730–1230 cm^{-1} (bottom), the ATR-FTIR spectra in Fig. 1a confirm the functionalization of glass surfaces with VTCS and ATCS. The spectrum of the pristine glass shows no prominent peaks associated with specific functional groups, indicating their absence on the surface. In the pristine glass, the peak at 1630 cm^{-1} is attributed to the bending vibration of adsorbed molecular water (δ H–O–H).[62,63] This band is observed in the spectra of VTCS-modified glass surfaces. After functionalization with DSH, the intensity and position of the H–O–H bending vibration remain relatively unchanged. In the case of ATCS-modified samples, this peak overlaps with the C═C stretching vibration at 1632 cm^{-1}, making it difficult to determine whether molecular water is still present. These observations indicate that water molecules may be re-adsorbed from ambient humidity, even after surface modification. The VTCS-modified glass spectrum indicates two separate C–H stretching peaks, likely influenced by Fermi resonance and combination bands involving the C═C stretch and C–H bending modes.[61] The peak at 3062 cm^{-1} corresponds to the asymmetric C–H stretching vibration of the vinyl group, while the peak at 2984 cm^{-1} represents the symmetric C–H stretching of the vinyl group. The peaks at 3024 cm^{-1} and 2958 cm^{-1} are assigned to symmetric and asymmetric C–H stretching of the vinyl group, respectively. Further, the peak at 1602 cm^{-1} corresponds to C═C stretching vibration, confirming the presence of vinyl groups. The peaks at 1409 cm^{-1} and 1276 cm^{-1} are attributed to in-plane deformations and bending modes of $=CH_2$ and =CH bonds, respectively.

On the other hand, while there is no literature precedent for the infrared spectroscopic characterization of ATCS molecules attached to glass surfaces, most studies have focused on the pristine forms of ATCS or VTCS[64–69] or their fixation to other substrates, such as aluminum,[70] mica,[58] or silicon wafers.[71] Similarly, the FTIR spectrum of ATCS-modified glass exhibits the characteristic vibrational modes that confirm the covalent bonding of allyl groups. As shown in Fig. 1a, the peaks at 3082 cm^{-1} and 2977 cm^{-1} are attributed to $=CH_2$ stretching, while the peak at 2930 cm^{-1} corresponds to CH_2 asymmetric stretching. The peak at 1632 cm^{-1} is assigned to C═C stretching. Additionally, the peaks at 1452 cm^{-1} and 1419 cm^{-1} are associated with CH_2 bending vibration, with the peak at 1387 cm^{-1} corresponding to $=CH_2$ bending. The peak at 1265 cm^{-1} represents the CH_2 bending modes of the terminal $=CH_2$ groups. These absorptions confirm the covalent bonding of vinyl and allyl groups from VTCS and ATCS onto the glass surface.

Functionalization of the VTCS- and ATCS-modified glass surfaces

The terminal alkene groups in VTCS- and ATCS-modified glass surfaces enable versatile modifications through thiol–ene click

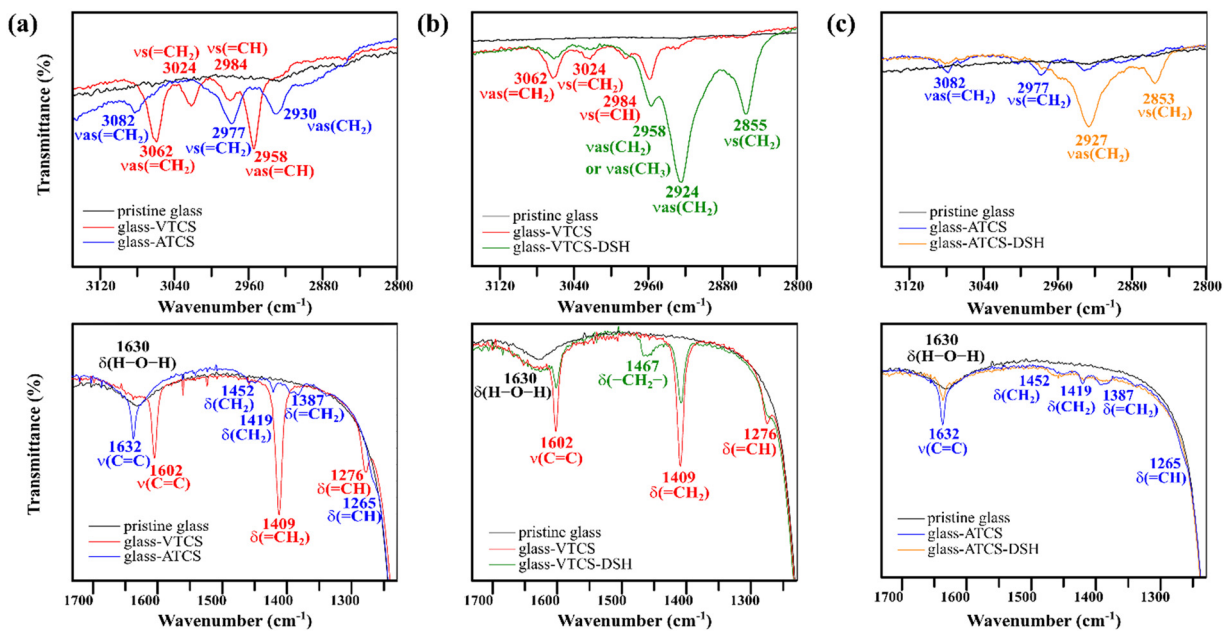

Fig. 1 ATR-FTIR spectra of (a) pristine glass, VTCS-, and ATCS-modified glass showing characteristic peaks of the vinyl and allyl groups. Transmittance spectra of VTCS- (b) and ATCS-coated glass surfaces (c) after functionalization with DSH, highlighting changes in peak intensities. The partial reduction in C═C stretching vibrations (1602 cm^{-1} for VTCS and 1632 cm^{-1} for ATCS) confirms the partial conversion of surface alkenes, indicating successful but incomplete functionalization.

© 2026 The Author(s). Published by the Royal Society of Chemistry

Open Access Article. Published on 02 September 2025. Downloaded on 2/12/2026 8:12:20 PM. This article is licensed under a Creative Commons Attribution 3.0 Unported Licence.

chemistry. This approach allows fine surface functionalization without compromising the integrity of the coating while simultaneously improving coating stability. Significant changes were observed following the thiol–ene click reaction between the VTCS-modified glass surface and DSH (Fig. 1b). Two new peaks at 2924 cm^{-1} and 2855 cm^{-1} are observed, corresponding to asymmetric and symmetric C–H stretching in methylene groups. These peaks are characteristic of the alkyl chain from DSH incorporated during the functionalization reaction. An increase in peak intensity at 2958 cm^{-1}, associated with the asymmetric CH stretching in the $–CH_2$ groups, was also observed. This increase in intensity is likely due to the asymmetric stretching of alkyl groups (methylene or methyl) from the DSH chains. A new peak at 1467 cm^{-1}, attributed to the deformation of newly formed $–CH_2–$ groups, indicates the successful conversion of some of the C═C bonds to C–C bonds. Concurrently, a decrease in the peaks at 3062 cm^{-1}, 3024 cm^{-1}, 2984 cm^{-1}, 1602 cm^{-1}, 1409 cm^{-1}, and 1276 cm^{-1} were noted, further confirming the partial conversion of surface alkenes and the fixation of the DSH molecules on the VTCS-modified glass surface. The partial conversion of surface alkenes was further supported by the persistence of the characteristic C═C peaks after functionalization, as a complete reaction would have resulted in the total disappearance of such peaks.

Similarly, distinct changes were observed in the IR spectrum of ATCS-modified glass surface upon its reaction with DSH (Fig. 1c). The spectrum shows a new peak at 2853 cm^{-1}, indicative of symmetric C–H stretching vibrations in the methylene groups, while the intensity of the peak at 2927 cm^{-1} increases, corresponding to asymmetric C–H stretching in the methylene groups. These peaks are characteristic of the alkyl chains introduced by DSH during the click reaction. Simultaneously, slight decreases in the peak intensities at 1632 cm^{-1}, 1419 cm^{-1}, 1387 cm^{-1}, and 1268 cm^{-1} are observed. These reductions likely result from the partial conversion of C═C bonds into C–C bonds during the click reaction. The increase in peak intensity at 1452 cm^{-1} is associated with CH_2 bending and thus confirms the covalent bonding of alkyl chains from DSH. The spectral changes in the VTCS and ATCS systems after reacting with DSH exhibit distinct differences. In addition, the incomplete disappearance of VTCS and ATCS original peaks suggests that only a certain percentage of alkene functionalities were reacted with DSH during the click reaction. The VTCS system shows more pronounced spectral changes, suggesting a greater extent of thiol–ene click reaction. In contrast, the changes in the ATCS system are relatively less significant, indicating a more limited reaction. This may be attributed to numerous factors, such as steric hindrance and accessibility of the reactive groups.

Light interaction and nanoscale topography

Developing hydrophobic or superhydrophobic coatings for practical use is often challenging due to the need to balance surface roughness with optical transparency.[72,73] An increase in surface irregularities would increase water repellency but simultaneously lower the optical performance due to the enhanced light scattering effect.[74] Achieving optimal balance between both properties requires precise control over the surface topography. This balance can typically be achieved when the surface features are kept below $\frac{1}{4}$ of the visible light wavelength range (400–800 nm) and ideally below 80 nm.[75–77] In practice, transparency is measured in terms of transmittance using UV-vis spectroscopy. Another crucial parameter is the fraction of the incident light lost due to scattering and reflection, which is a function of the surface roughness and abrupt changes in refractive index at the interfaces.[14,76]

Fig. 2 demonstrates the optical properties of the modified glass surfaces before and after functionalization. The average transmittance of the pristine glass substrate is 92%, with approximately 8% of incident light lost due to reflection. VTCS and ATCS coatings improved the average transmittance of the substrate by ~3.0% and ~1.0%, respectively at 550 nm (Fig. 2a and b top). DSH functionalization further enhanced the optical transmittance of both modified substrates. The VTCS-modified substrate had an enhancement in transmittance of ~3.7% (Fig. 2a top), while for the ATCS-modified substrate, the enhancement was ~1.4% (Fig. 2b top) at 550 nm. Comparable optical improvements have been reported in earlier studies.[46,75,78,79] Li and co-workers[43] reported a multifunctional surface where VTCS was polymerized on glass. Their surface maintained about 83% transparency above 400 nm, comparable to their reference glass. Our results demonstrate superior optical performance compared to this previous study. Reflectance data (Fig. 2a and b bottom) revealed a reduction for both VTCS- and ATCS-modified glass substrates. Furthermore, VTCS modification resulted in an average reflectance reduction of ~3.6% (Fig. 2a bottom), while ATCS modification led to an average decrease of ~1.4% at 550 nm (Fig. 2b bottom). DSH functionalization further decreased reflectance by ~4.3% for the VTCS-modified glass and ~1.5% for the ATCS-modified glass at 550 nm. The observed decrease in reflectance is attributed to the antireflective properties of the films.[80] This is likely due to the low refractive indices of the coatings ($n_{VTCS} \approx 1.43$ and $n_{ATCS} \approx 1.44$) and their morphology, which together create a gradient interface between air ($n \approx 1$) and glass ($n \approx 1.5$).

Water contact angle (WCA) measurements were carried out to characterize the wettability of the studied surfaces. The WCA of pristine glass is 26° ± 6. The VTCS-modified glass surface exhibited superhydrophobic behavior with a WCA of 168° ± 2 and a sliding angle of 2°. After functionalization with DSH, the samples exhibited a WCA of 170° ± 4 with a sliding angle of 1°. This was achieved despite the absence of perfluoroalkyl chains, which are known for their low surface energy and ability to enhance hydrophobicity.[81,82] In contrast, ATCS-modified glass showed WCAs of 109° ± 4 and 113° ± 4 before and after functionalization with DSH, respectively. These negligible contact angle changes likely reflect the fact that the additional, chemically grafted DSH layer does not substantially alter the surface energy, particularly when DSH chains are embedded

Open Access Article. Published on 02 September 2025. Downloaded on 2/12/2026 8:12:20 PM.
This article is licensed under a Creative Commons Attribution 3.0 Unported Licence.

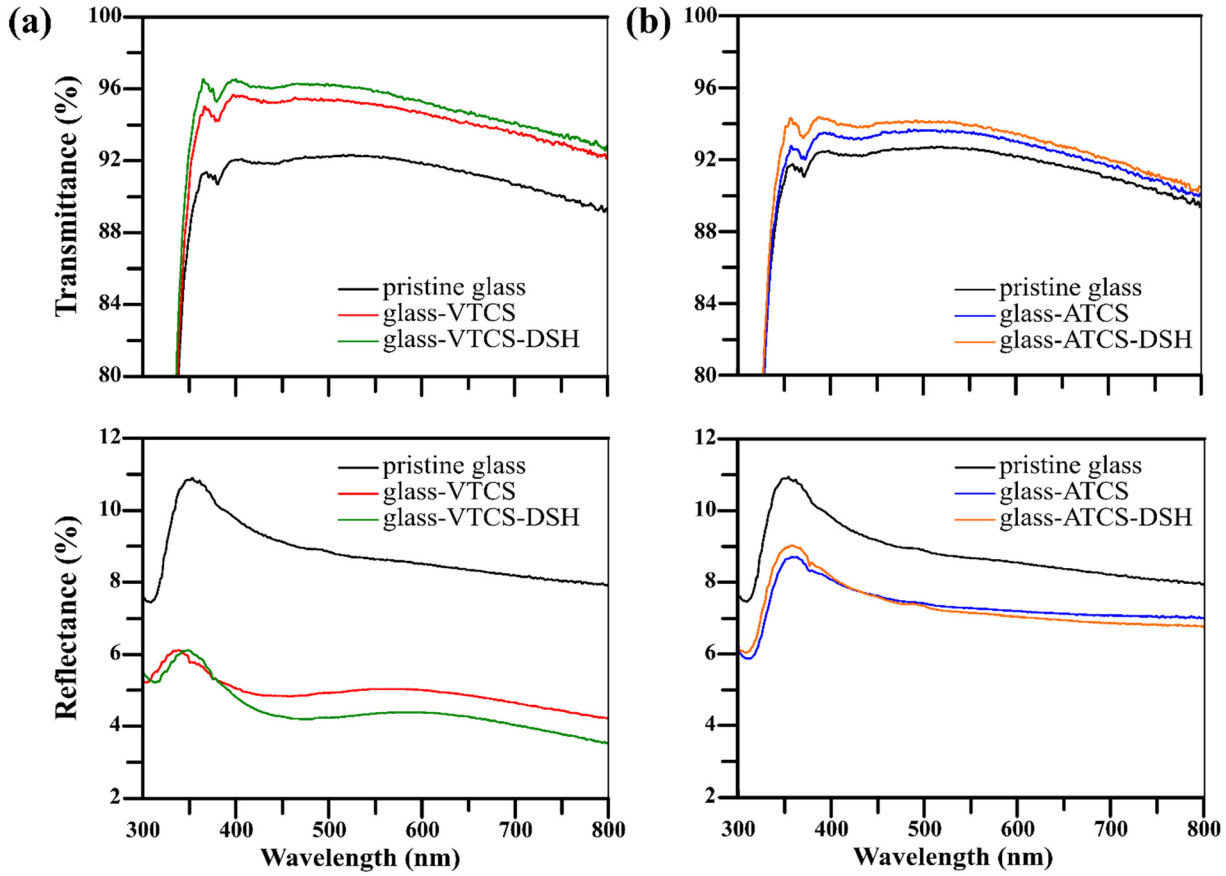

Fig. 2 UV-vis transmittance and reflectance spectra of VTCS- and ATCS-modified glass before and after functionalization. (a) VTCS-modified glass (top) transmittance and (bottom) reflectance spectra. (b) ATCS-modified glass (top) transmittance and (bottom) reflectance spectra. In each panel, spectra of the modified surfaces ae shown with the pristine glass for comparison.

within the coating network or when thiol coverage, as in our case, is modest. Moreover, AFM measurements (Table 1) show only minor variations in surface roughness after functionalization, indicating that the surface morphology, an important determinant of wettability, was largely preserved. Finally, it is worth noting that contact angle measurements are inherently less sensitive than spectroscopic methods to subtle changes in surface chemistry, especially when surface morphology and roughness remain essentially unchanged.

Despite these changes in wettability, both surfaces remained optically transparent. While longer alkyl chains generally increase hydrophobicity due to greater van der Waals interactions,[83] the slightly longer chain of ATCS may have introduced more conformational flexibility due to the additional methylene group. Infrared and Raman spectroscopy studies reported by several groups[68,70] indicated that only the gauche conformer was present in all three physical states of ATCS. This could potentially affect how molecules arrange on the surface, leading to less ordered structures, which may reduce hydrophobicity compared to VTCS. Fig. 3 shows the nanoscale surface topography and morphology of the modified glass surfaces before and after functionalization, along with the size distribution of the surface features. In the 2-dimensional (2D) AFM images (Fig. 3i-a), the VTCS-modified glass shows a nanofilament-like dense network. This is consistent with observations reported by Li and co-workers.[43] After functionalization with DSH (Fig. 3ii-a), these nanofilament-like structures become thicker, with less pronounced gaps in between and slightly increased roughness. In contrast, the ATCS-modified glass (Fig. 3iii-a) shows irregular agglomerated structures distributed across the surface, making the coating less uniform and smoother than the VTCS-modified surface. These features suggest that ATCS forms discrete domains instead of a continuous layer, resulting in a heterogeneous surface topography. After functionalization with DSH (Fig. 3iv-a), the aggregates become more defined. This change in topography gives evidence of a possible growth of the aggregates

Table 1 The roughness parameters of pristine and modified glass surfaces determined by AFM measurements

As prepared coatings	Mean roughness R_a (nm)	Root-mean-square roughness R_q (nm)
Pristine glass	1.1	1.3
Glass-VTCS	50.6	63.3
Glass-VTCS-DSH	50.2	64.2
Glass-ATCS	19.2	26.0
Glass-ATCS-DSH	25.6	37.9

© 2026 The Author(s). Published by the Royal Society of Chemistry

Open Access Article. Published on 02 September 2025. Downloaded on 2/12/2026 8:12:20 PM.
This article is licensed under a Creative Commons Attribution 3.0 Unported Licence.

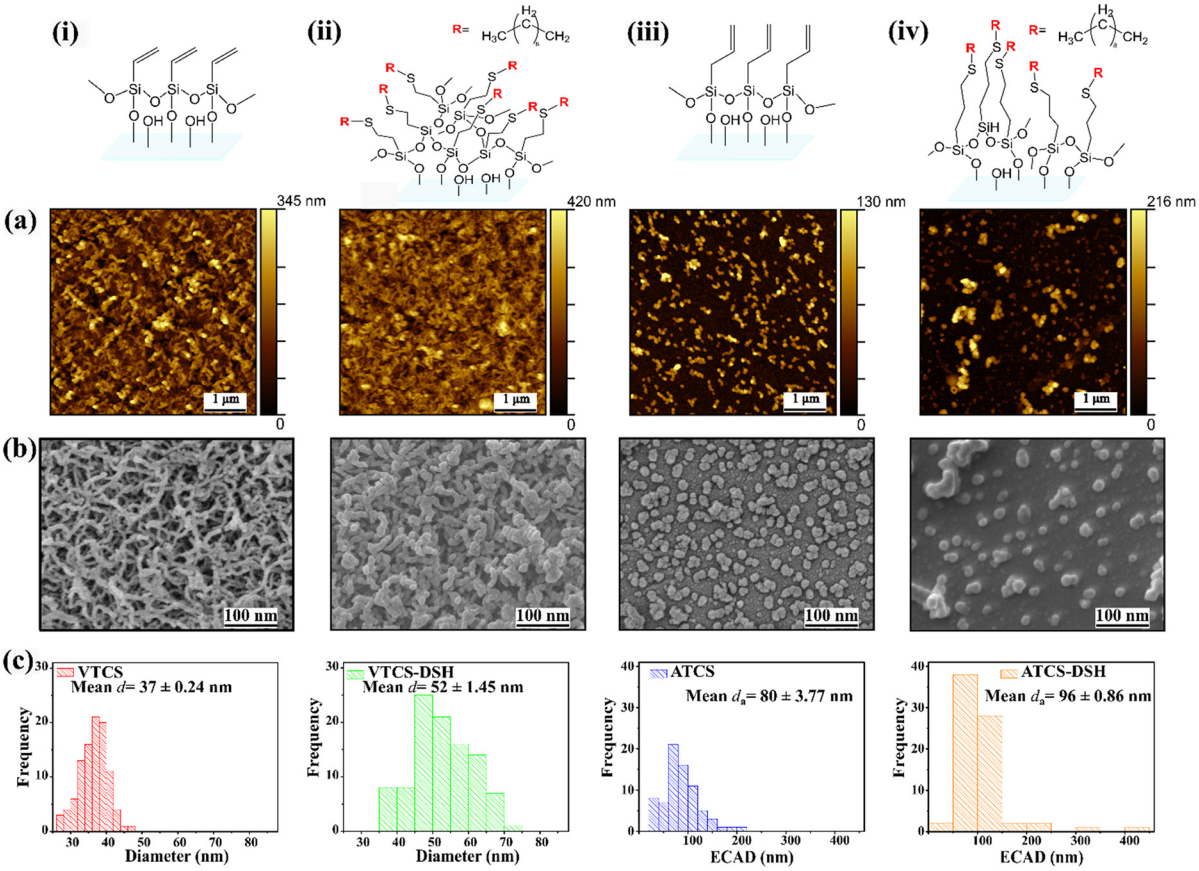

Fig. 3 Surface characterization of VTCS- and ATCS-modified glass before and after functionalization. Molecular structures of (i) VTCS, (ii) VTCS-DSH, (iii) ATCS, and (iv) ATCS-DSH. (a) 2D AFM images of VTCS- and ATCS-modified glass surfaces (i and iii) before and (ii and iv) after functionalization. (b) SEM images showing scale bars of 100 nm. (i and ii) VTCS-modified glass with nanofilaments and (iii and iv) ATCS-modified glass with particle-like morphology, both before and after functionalization. (c) Size distribution of (i and ii) VTCS nanofilaments and (iii and iv) ATCS particles, both before and after functionalization.

after thiol–ene click reaction by increased molecular interactions in the modified regions.

SEM images (Fig. 3b) further confirm these observations, revealing a well-defined nanofilament network for VTCS (Fig. 3i-b and ii-b), which generates a highly porous surface instead of a densely packed coating. The size distribution analysis (Fig. 3i-c) indicates a relatively narrow filament diameter size range between 32 and 42 nm with an average diameter of 37 ± 1 nm. These results explain our superior optical performance compared to those reported by Li and co-workers,[43] whose silicon nanofilaments measured ~30–50 nm in diameter. Furthermore, the notable reflectance reduction from 8.6% for pristine glass to 5.0% and 4.4% at 550 nm achieved by the VTCS-modified glass before and after functionalization, respectively, is primarily attributed to its porous nanofilament network.[84] This network reduces the abrupt refractive index change between glass and air. It creates a gradual index transition, minimizing Fresnel reflections through effective index matching, thereby enhancing the optical performance of the glass surface.[80] Similar improvements have been reported for polymethylsiloxane nanofilament coating, with filament diameters of 20 to 50 nm, where ellipsometry revealed a refractive index as low as 1.12.[49] After functionalization with DSH (Fig. 3ii-c), the diameter distribution shifted towards larger sizes, with most filaments measuring between 45 to 65 nm and an average diameter of 52 ± 2 nm. The measured sub-65 nm diameters of these porous nanofilaments further confirm their role in reducing the reflected fraction of visible light and enhancing transparency.[85] The high surface roughness of the porous VTCS nanofilament network (Table 1) contributes significantly to the surface architecture, supporting the development of the observed superhydrophobic behavior, which is discussed in detail in a later section.[85]

ATCS (Fig. 3iii-b) shows a distribution of irregular agglomerates with smaller particle-like structures across the surface, which is suspected to be a thinner coating than the layer underneath the aggregate features (Fig. S2). The equivalent circular area diameter (ECAD)[86] is defined as the diameter of the particle's projected image based on its area and is represented by (d_a). The ECAD of ATCS-glass particles exhibits a broad distribution, with most particles having a diameter below 150 nm and a few extending up to 210 nm (Fig. 3iii-c). This reflects the heterogeneous nature of the ATCS coating with an

Open Access Article. Published on 02 September 2025. Downloaded on 2/12/2026 8:12:20 PM.
This article is licensed under a Creative Commons Attribution 3.0 Unported Licence.

average ECAD of around 80 ± 4 nm. The d_a was calculated using the following equation:

$$d_a = 2 \times \sqrt{(A/\pi)} \quad (1)$$

where A is the area of the particle measured by ImageJ, representing the number of pixels or calibrated unit (nm) within the particle boundary.

Following functionalization with DSH, the particle distribution becomes more concentrated around 100 nm, with a few particles extending up to 425 nm, suggesting further aggregation growth. The particle ECAD distribution (Fig. 3iv-c) shows a narrower range, with most particles still below 150 nm and a mean diameter of approximately 96 ± 1 nm. This suggests shifting towards slightly larger particles after the click reaction. Roughness parameters, measured by AFM analysis, presented in Table 1 for the VTCS- and ATCS-modified surfaces before and after functionalization provide valuable insights into the evolution of surface topography. The VTCS-modified surfaces, characterized by a porous nanofilament network, show minor changes upon functionalization. The relatively constant mean roughness (R_a) (from 50.6 nm to 50.2 nm) and root mean square roughness values (R_q) (from 63.3 nm to 64.2 nm) indicate that the general network structure was preserved upon functionalization. On the other hand, the functionalization resulted in more pronounced changes for the ATCS-modified surfaces. While the R_a values remain relatively constant (26.0 nm to 25.6 nm), the R_q increased significantly (19.2 nm to 37.9 nm). This increase suggests that the functionalization caused more pronounced surface features due to aggregate growth or coalescence without altering the average surface height.

Chemical mapping and spectral analysis of surface modification using photo-induced force microscopy (PiFM)

Infrared results highlighted the need for a more sensitive quantitative technique to investigate surface chemistry and accurately quantify the functionalization reaction conversion

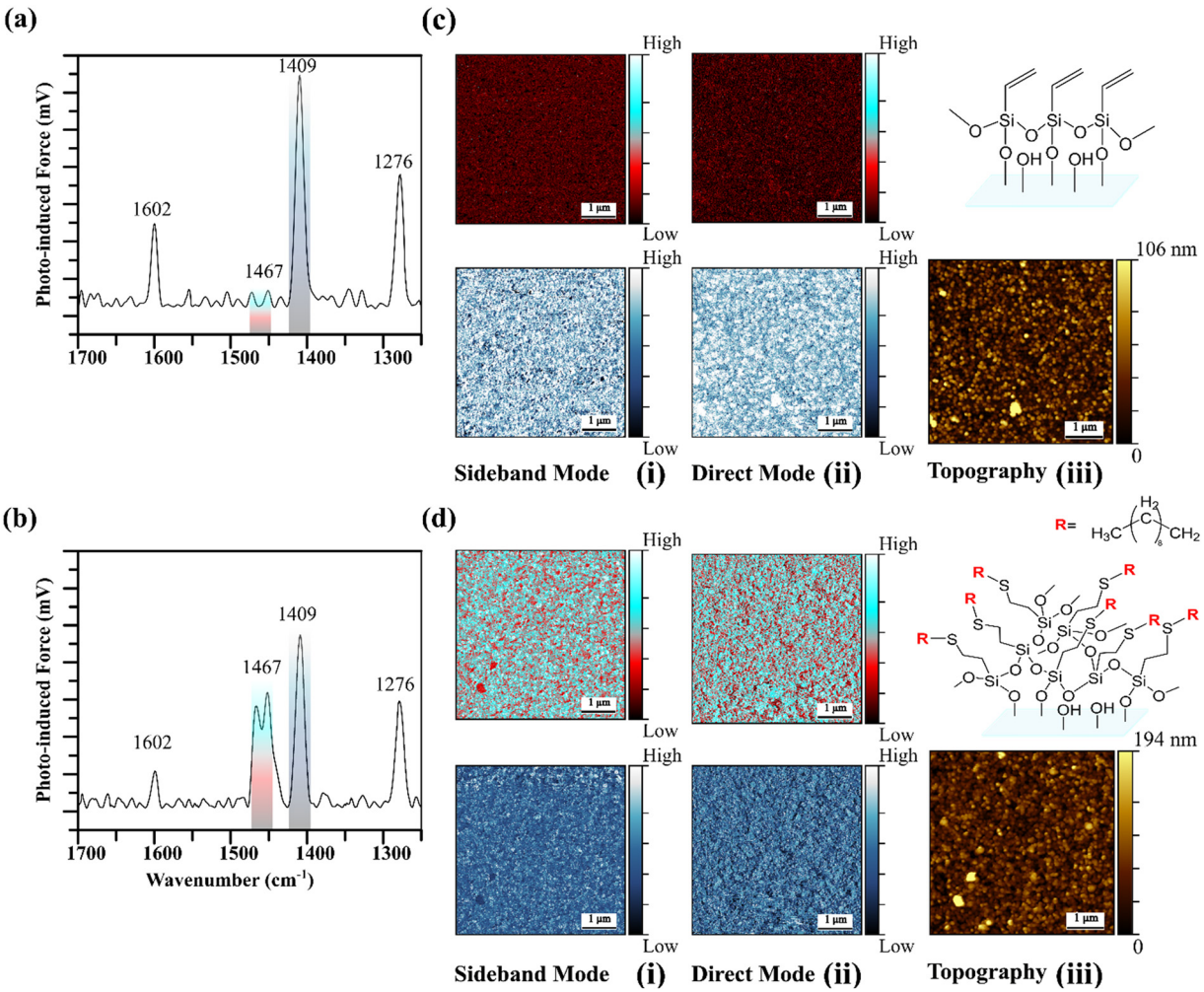

Fig. 4 PiFM spectra, chemical mapping, and topography images of glass surfaces modified with VTCS. PiFM spectra of VTCS-modified glass before (a) and after (b) thiol–ene click reaction. PiFM chemical mapping images before (c) and after (d) functionalization, collected at 1467 cm^{-1} and 1409 cm^{-1} in (i) sideband and (ii) direct modes. (iii) Topography images of the corresponding analyzed surface.

© 2026 The Author(s). Published by the Royal Society of Chemistry

Open Access Article. Published on 02 September 2025. Downloaded on 2/12/2026 8:12:20 PM.
This article is licensed under a Creative Commons Attribution 3.0 Unported Licence.

of the studied surfaces. In this context, PiFM[87–89] local point infrared spectroscopy was selected as an emerging technique to support our initial findings. This technique represents a high-resolution spectroscopy technique, enabling the observation and mapping of chemical changes with nanoscale resolution and offering a complete investigation of the functionalization process. It should be noted that local point infrared spectral acquisitions were collected over all the analyzed surfaces, and an average of these spectra was then presented. Bare soda-lime glass produced a distinct mid-infrared PiFM spectra with no visible peaks in the 1700–1250 cm^{-1} range (Fig. S5a). The PiFM local point infrared spectra of VTCS- and ATCS-modified glass surfaces (Fig. 4a and b and 5a and b, respectively) showed peaks attributed to the stretching and bending vibrations of the vinyl (1602 cm^{-1}, 1467 cm^{-1}, 1409 cm^{-1}, and 1276 cm^{-1}) and allyl (1632 cm^{-1}, 1452 cm^{-1}, 1387 cm^{-1}, and 1265 cm^{-1}) groups. These findings were in good agreement with the ATR-FTIR spectroscopy results for both samples (Fig. 1) and further supported the expected functional groups on the modified glass surfaces. Notably, the absence of a peak around 1467 cm^{-1} (Fig. 4a) indicates the absence of C–C single bonds in the initial VTCS structure. Significant spectral changes are observed following the thiol–ene click reaction with DSH (Fig. 4b), providing additional evidence for the partial surface functionalization. The intensity of the C═C stretch decreased considerably, indicating the consumption of a certain percentage of the vinyl groups. The peaks at 1409 cm^{-1} and 1276 cm^{-1} also decreased with approximately the same range, further confirming the loss of C═C functionality and suggesting that these double bonds have been converted into C–C bonds upon thiol–ene click reaction. The appearance of a new peak at 1467 cm^{-1} provides additional evidence for this conversion, signifying the presence of CH_2 groups in C–C single bonds.

To evaluate the spatial distribution of the DSH functionalization in VTCS and ATCS films, we performed PiFM chemical mapping in both sideband and direct modes. As

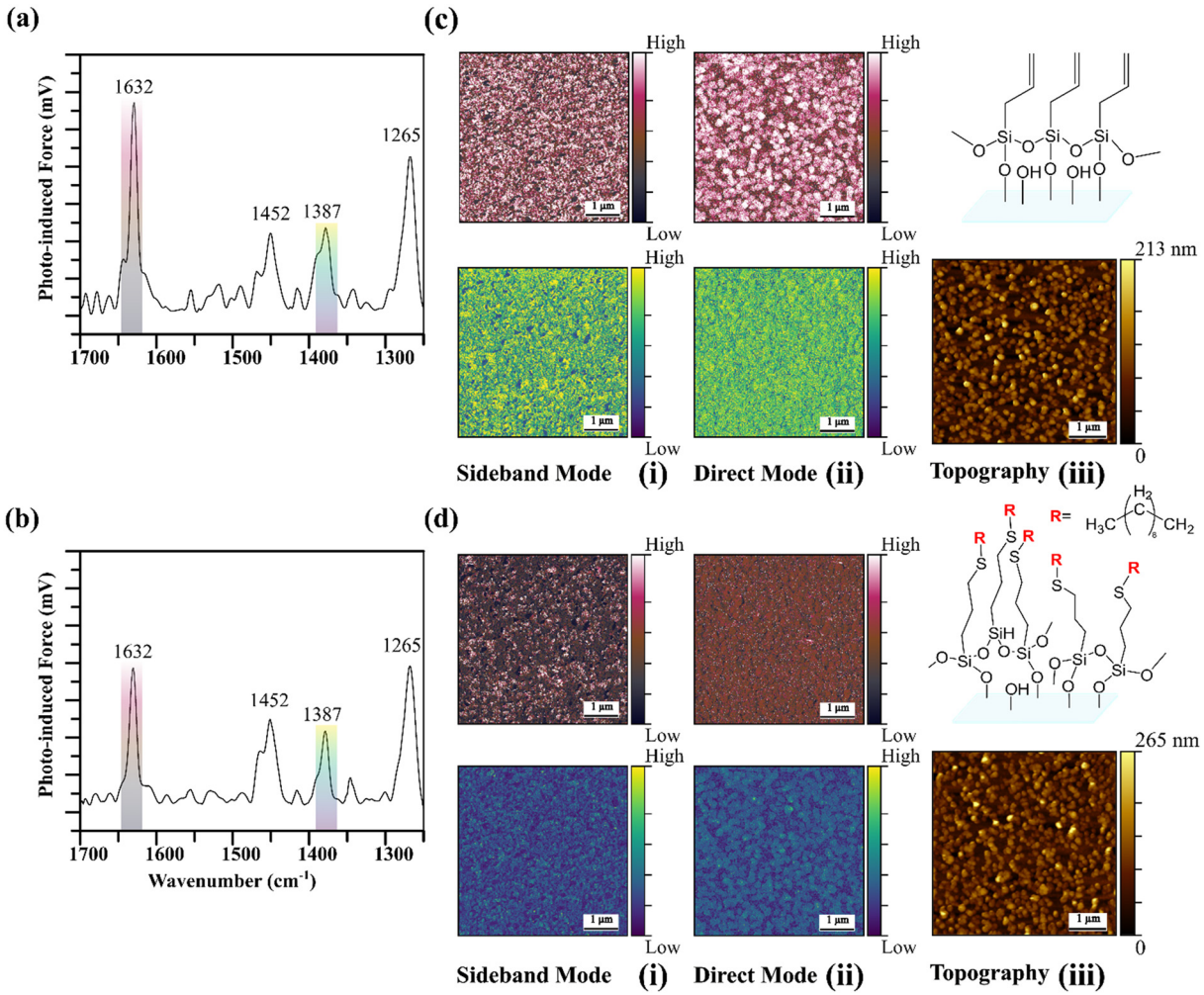

Fig. 5 PiFM spectra, chemical mapping, and topography images of glass surfaces modified with ATCS. PiFM spectra of ATCS-modified glass before (a) and after (b) thiol–ene click reaction. PiFM chemical mapping images before (c) and after (d) functionalization, collected at 1632 cm^{-1} and 1378 cm^{-1} in (i) sideband and (ii) direct modes. (iii) Topography images of the corresponding analyzed surface.

Open Access Article. Published on 02 September 2025. Downloaded on 2/12/2026 8:12:20 PM. This article is licensed under a Creative Commons Attribution 3.0 Unported Licence.

expected, since the PiFM spectrum of bare soda-lime glass did not show any signals overlapping with those of VTCS or ATCS, the corresponding PiFM maps of its surface displayed uniformly low intensity, as illustrated in Fig. S4b at the C═C band (~1632 cm^{-1}). The resulting chemical maps (Fig. 4c and d; 5c and d; S3c and d; and S4c and d) revealed a distinct contrast between the control and functionalized samples, providing supported evidence of successful functionalization occurring both at the surface and within the film depths. High-intensity zones in these maps correlated with the locations of filament-like structures and particles observed in the topography scans of VTCS- and ATCS-modified glass surfaces, respectively.

For VTCS-modified surfaces (Fig. 4c and d), pre-functionalization maps at 1409 cm^{-1} (δ(═CH_2)) showed higher contrast in the sideband mode (Fig. 4ci) compared to the direct mode (Fig. 4cii). The in-depth mode (Fig. 4cii) reveals a more uniform filament-like structure with high-intensity signal distribution, representing areas rich in vinyl groups. However, gaps between these structures indicate regions with lower molecular concentrations. Post-functionalization maps, collected at 1409 cm^{-1} (δ(═CH_2)) (Fig. 4d), 1276 cm^{-1} (δ(═CH)) (Fig. S3), and 1602 cm^{-1} (ν(C═C)) (Fig. S3), show a decrease in intensity, particularly in the areas surrounding the features. This indicates that the regions originally rich in C═C bonds have been effectively converted, leaving fewer double bonds and a more uniform surface. A similar pattern is observed at the surface level, with homogeneous functionalization indicating good molecular permeability of the molecules as they diffused into the VTCS layer. These findings confirm the successful functionalization of the modified glass surface both at the surface level and within the film. In contrast, ATCS-modified glass (Fig. 5a and b) demonstrated moderate changes in the peak intensities. Following the functionalization reaction (Fig. 5b), we observed a mild decrease in peak intensities at 1632 cm^{-1} (ν(C═C)), 1265 cm^{-1} (δ(═CH)), and 1387 cm^{-1} (δ(═CH_2)), indicative of the partial loss of C═C bonds. Concurrently, the increase in intensity of the preexisting peak at 1452 cm^{-1} (δ(CH_2)) supports the formation of C–C bonds resulting from the thiol–ene reaction with DSH. These spectral changes provide strong evidence for the partial thiol–ene click reaction.

To confirm the uniformity of the functionalization across the ATCS-modified surfaces, we also employed PiFM in sideband (Fig. 5ci) and direct modes (Fig. 5cii) analyses. Before functionalization (Fig. 5c), in-depth and surface PiFM mapping revealed that the entire substrate is uniformly coated, not just regions with visible aggregates. The in-depth PiFM maps collected at 1632 cm^{-1} (ν(C═C)) (Fig. 5cii) and 1265 cm^{-1} (δ(═CH)) (Fig. S4) show a higher signal intensity in the aggregate regions due to the higher molecular concentration in these areas compared to the surrounding surface areas. However, surface mapping reveals a relatively more homogeneous signal distribution with low-intensity signals in the regions between aggregates. The underneath layer is composed of a lower molecular concentration than the aggregates. After functionalization (Fig. 5d), the PiFM images collected at 1632 cm^{-1} (ν(C═C)), 1387 cm^{-1} (δ(═CH_2)), and 1265 cm^{-1} (δ(═CH)) (Fig. S4) show a decrease in signal intensity, while certain regions remained at high intensity uniformly across the surface. The in-depth PiFM results (Fig. 5dii) further support this finding, as the signal intensity, pre-functionalization was initially localized to the aggregates becomes more evenly distributed across the surface. However, some regions exhibit lower saturation levels compared to the pre-functionalized surface (Fig. 5cii). This indicates that certain C═C bonds remain unconverted across the substrate. This confirms that functionalization occurred at both levels: on the aggregates and surrounding areas across the entire substrate, with some C═C bonds remaining unconverted. These results provide valuable insights into surface chemistry and the distribution of the functionalization.

Why does VTCS form porous nanofilament networks but not ATCS?

Previous research on VTCS coatings has been limited, with only a few studies exploring their potential for creating 3D nano-architectures. Rollings and co-workers[71] as well as Rollings and Veinot[59] were the first to investigate VTCS as a coating, reporting the formation of nanofibers through surface-induced vapor-phase polymerization on silicon wafers. Later on, Li and co-workers[43] demonstrated the formation of VTCS-porous nanofilaments through the phase separation technique on glass substrates. It is known that under optimized conditions, organosilanes condense with water and surface silanols, creating covalently attached, crosslinked polymeric layers through vertical polymerization.[15] In our study, VTCS condensation with water and glass surface silanols resulted in a porous nanofilament network. This has likely occurred due to the covalent bonding of VTCS followed by crosslinking into polymeric layers through vertical polymerization. Among the key factors governing the production of nanofibers are the concentration of the surface hydroxyl groups and the adsorbed water layer, which serve as nucleation sites for vertical polymerization.[59]

Under ambient conditions in our study, when VTCS is introduced to the reaction vial, it hydrolyzes either in solution or upon adsorption on the glass substrate.[18,44,90] Subsequently, the hydrolyzed VTCS is attached to the surface due to the condensation reaction of its one (or possibly more) silanol groups with the glass hydroxyl groups. At this point, the remaining silanol groups are available for coupling with other physisorbed hydrolyzed VTCS moieties.[18] Subsequently, the alkyl chains of each VTCS crosslinking must rearrange into a configuration that minimizes their interaction from overlapping van der Waals radii (3.5 Å).[91] This is because the maximum bond length of a Si–O–Si, even when stretched to its limit, is 3.2 Å.[92] The residual hydroxyl groups maintain specific orientation away from the substrate to guide further condensation reactions with other hydrolyzed VTCS moieties.[91] The nanofilament growth is initiated by the first

© 2026 The Author(s). Published by the Royal Society of Chemistry

Open Access Article. Published on 02 September 2025. Downloaded on 2/12/2026 8:12:20 PM.
This article is licensed under a Creative Commons Attribution 3.0 Unported Licence.

anchored hydrolyzed VTCS, followed by the nucleation site. Therefore, vertical polymerization produces a porous cross-linked nanofilament network. Hence, the key point for nanofilament formation is the initial nucleation and subsequent vertical growth of the polymeric islands perpendicular to the surface.[59] In contrast, research on ATCS coatings is even more limited. Li and Horton,[58] studied the assembly process of ATCS on mica under an inert atmosphere to minimize the water vapor effect on the polymer formation in the monolayers. They found that, at room temperature, ATCS forms homogeneous and continuous overlayers of only 1 to 2 molecules thick. At −78 °C, polymerized aggregates formed due to water condensation within the reaction chamber. Additionally, nanoindentation technique was employed to evaluate the mechanical properties of the coatings, distinguishing between ordered SAM and polymerized aggregates on the surface. In our study, both VTCS and ATCS have double bonds at the end of their alkyl chain. However, ATCS contains an additional methylene group, leading to a slightly longer chain with increased flexibility. While VTCS readily forms nanofilaments, ATCS exhibits different assembly due to its structural constraints. The additional methylene group introduces steric hindrance which combined with the formation of charged centers due to the partial C═C polarization, disrupts the lateral crosslinking required for filament growth.[58] Instead, ATCS adopts two distinct morphologies, an ordered SAM and irregular polymerized aggregates, which were suggested to be physiosorbed in the nanoindentation study of Li and Horton.[58]

Quantification of the thiol–ene click reaction conversion

The peak integration method was applied to both ATR-FTIR and PiFM spectra (Fig. 6) to quantify the thiol–ene click reaction conversion. The method involves measuring the area under the peaks associated with the C═C bond before and after functionalization. The conversion (%) of the thiol–ene click reaction is then calculated using the following equation:

$$\text{Conversion (\%)} = ((A_{\text{initial}} - A_{\text{final}})/A_{\text{initial}}) \times 100 \quad (2)$$

where A_{initial}, represents the area of the C═C peak before functionalization, and A_{final} after functionalization.

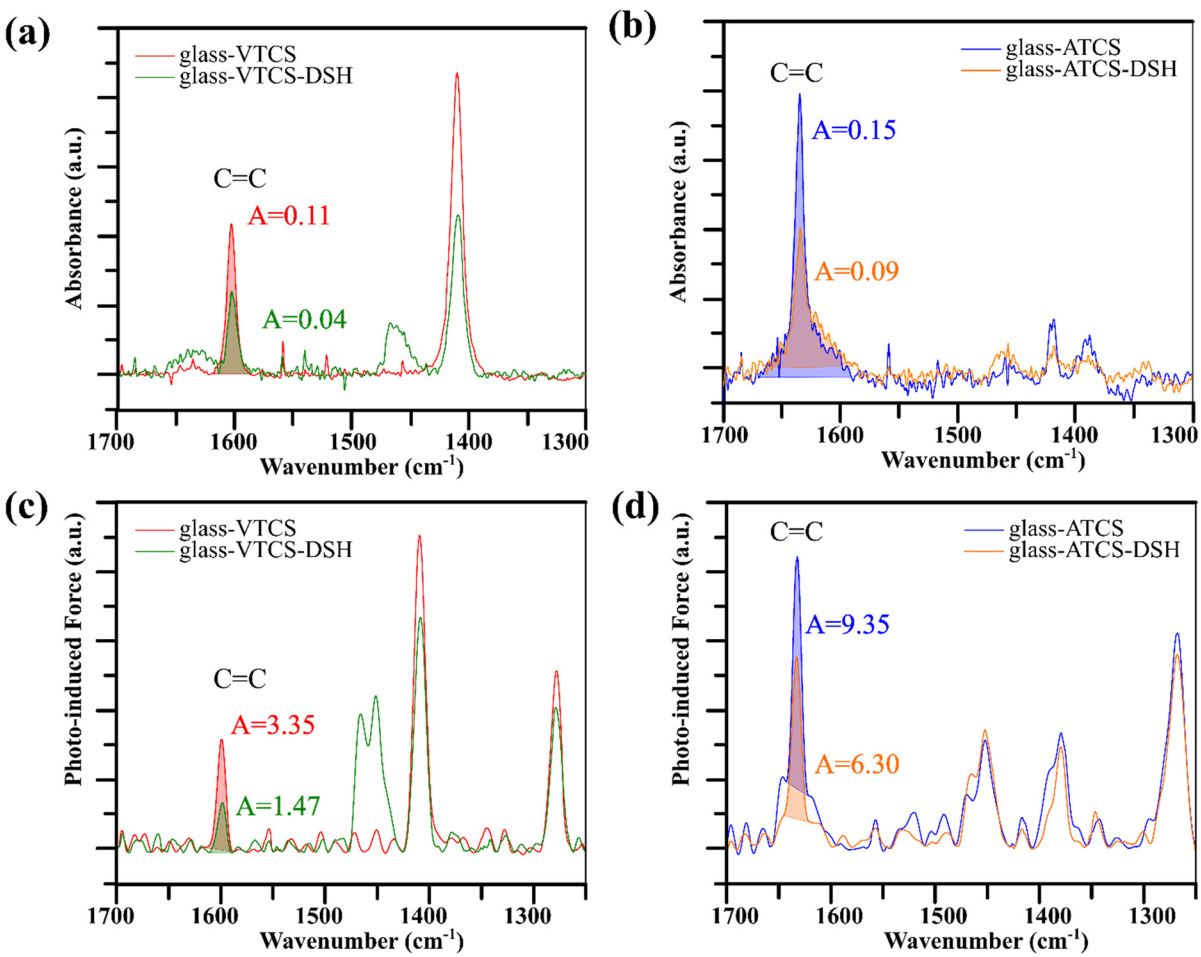

Fig. 6 Quantifying the thiol–ene click reaction conversion *via* ATR-FTIR (a and b) as well as PiFM (c and d) spectra of VTCS- and ATCS-modified glass before and after functionalization. (a and c) VTCS- and (b and d) ATCS-modified surfaces, highlighting the C═C bond peak area reduction.

Open Access Article. Published on 02 September 2025. Downloaded on 2/12/2026 8:12:20 PM. This article is licensed under a Creative Commons Attribution 3.0 Unported Licence.

Based on ATR-FTIR analysis, the click reaction conversion was estimated to be approximately 63% and 40% for VTCS- and ATCS-functionalized glass surfaces, respectively. These values are slightly higher than those obtained *via* PiFM analysis which yielded conversions of about 56% and 33% for VTCS- and ATCS-functionalized glass surfaces, respectively. This difference is attributed to differences in resolution and sampling depth between the two techniques.

Thiol–ene click reaction is widely used as a general route to functionalize organosilanes for surface coating applications.[43] This reaction is typically known for its high efficiency, resulting in quantitative to near-quantitative yields.[93,94] The conversion values obtained in our study from both ATR-FTIR and PiFM are relatively low, which is unexpected for this reaction. While Li and co-workers[43] performed click reactions of glass substrates bearing vinyl groups, they did not provide quantitative analysis of the reaction yields. In contrast, Campos and co-workers[95] achieved 45–75% surface coverage for multiple functional thiols attached to alkene-terminated oxide-free Si(111) substrates *via* thiol–ene click chemistry. This reaction is typically known for its high efficiency, resulting in quantitative to near-quantitative yields.[93,94] Our click reaction conversions for VTCS and ATCS are relatively low at 56% and 33%, respectively, which is unexpected for this reaction. Furthermore, Zhang and co-workers[96] have employed wettability measurements to confirm the covalent bonding of diverse thiols to an allyl-containing copolymer grafted onto metal surfaces. Additionally, the researchers demonstrated the practical efficiency of the coating by applying it to a porous membrane. They achieved 99.2% separation efficiency, which also confirmed the functionalization's effectiveness. Kaczmarek and co-workers[94] reported a successful reaction, as evidenced by the total disappearance of the characteristic peaks corresponding to thiol and the C=C stretching vibration of polyether. However, their reaction was performed at the molecular level, which likely facilitated higher efficiency.

Similarly, the study by Tucker-Schwartz and co-workers[93] involved the synthesis of fifteen trialkoxysilanes. These chemicals were produced by reacting either alkenes with mercaptoalkyltrialkoxysilanes or thiols with allyltrialkoxysilanes. The reaction was carried out in the presence of a photo-initiator in molecularly dissolved state. A key difference in our work was the heterogeneous nature of the reactions in solid–liquid interface and the use of a surface-sensitive approach to quantify the reaction yield. Unlike conventional techniques that provide averaged bulk signals, PiFM spectra deliver quantitative surface chemical information with molecular resolution. This high spatial sensitivity likely enabled us to distinguish between reacted and unreacted molecules, subtleties that earlier methods may have overlooked.

Furthermore, the reaction yields are highly dependent on the availability of surface-exposed C=C bonds. In the case of VTCS, the formation of nanofilaments during self-assembly on the glass surface likely traps a fraction of C=C bonds within the internal network, rendering them unavailable for subsequent reactions. Similarly, ATCS coating form aggregates with disordered arrangements, which may sterically obstruct access to a fraction of C=C bonds, preventing their reaction with decanethiol. However, the conversions were incomplete, likely due to steric hindrance preventing some double bonds that are buried within the polymerized VTCS nanofilaments and ATCS aggregates from reacting.

Thus, a fraction of alkene molecules not positioned at the coating–solution interface remain inaccessible to react with thiols due to limited molecular penetration. The lower conversion observed for ATCS (33%) compared to VTCS (56%) suggests that ATCS aggregates adopt a more compact morphology that buries allyl groups more effectively than the VTCS filament-network. Biggs and co-workers[97] have quantified polymer grafting efficiency on acrylate silane functionalized glass substrates through quartz crystal microbalance with dissipation (QCM-D) using gold, plain, and coated silicon sensors. They reported that steric hindrance was the limiting factor for poly[oligo(ethylene glycol)methyl ether methacrylate] grafting on gold sensors, while that of poly(*N*-isopropylacrylamide) was dependent on chain length. While the successful grafting on silicon-coated sensors had lower efficiency than that on gold, this was attributed to the acrylate group density and spacing. Thus, steric hindrance and molecules accessibility are decisive factors in thiol–ene reaction yields on functionalized glass surfaces.

Chemical stability and mechanical durability of the surfaces

VTCS-modified glass surfaces demonstrated superior properties to ATCS coatings, making them more promising candidates for practical applications. The VTCS coatings consist of a well-defined nanofilament network exhibiting desired transparency, superhydrophobicity, self-cleaning ability, and antireflective properties. In contrast, while ATCS coatings are transparent, they demonstrate hydrophobicity with lower contact angles. They are comprised of irregular structures, which may compromise their long-term performance. Consequently, we were interested in evaluating the chemical stability and mechanical durability of the prepared superhydrophobic VTCS-modified glass surfaces before and after functionalization with DSH through their static water contact angle.

The durability and stability testing comprised three protocols, each involving three freshly prepared samples tested over three successive cycles. Each cycle lasted 2 hours except for the thermal cycling test, where each cycle lasted for 6 h. Our protocols were guided by literature[8,98,99] and two testing standards for photovoltaic panels: ASTM B117-16[100] for immersion in an ionic solution and IEC 61215-2[101] for thermal cycling. We believe these test conditions are relevant for evaluating the durability of superhydrophobic surfaces on a laboratory scale. However, further refinement of the proposed protocols is welcomed to effectively assess the aging characteristics of different types of superhydrophobic surfaces at an industrial scale. Other parameters may also need to be considered for various applications.

© 2026 The Author(s). Published by the Royal Society of Chemistry

Open Access Article. Published on 02 September 2025. Downloaded on 2/12/2026 8:12:20 PM.
This article is licensed under a Creative Commons Attribution 3.0 Unported Licence.

To evaluate the durability of superhydrophobic surfaces under simulated environmental conditions, we developed a custom-designed waterfall-impact setup similar to that used in our previous study[56] with a moderate flow (4.3 mm h^{-1}) (equivalent to 4.3 mm h^{-1} over 1 m^2). All experiments were conducted under laboratory conditions at room temperature. The coating's resistance in an ionic environment was also examined. Before and after functionalization with DSH, three samples of the modified glass were submerged in a 5 wt% sodium chloride solution, following ASTM B117[100] guidelines for the salt spray testing standard. This solution's pH was measured at 5.7, simulating the combined effects of salt exposure and slightly acidic rainwater.[102] The samples were soaked in the solution for multiple cycles, rinsed with deionized water, and finally air-dried.

The waterfall impact test (Fig. 7a) shows a significant initial drop of contact angles from ~170° to ~140°, both before and after functionalization. Subsequently, this decrease reached and maintained a plateau at ~140° for the following three cycles. The initial contact angle of ~170° with the sliding angle of 2° confirms the Cassie–Baxter state, where air is trapped within the nanofilament network, enabling water repellency.[103,104] However, the significant decrease to ~140° and the observed droplet pinning during measurements suggest a transition toward the Wenzel state.[105] This suggests a loss of superhydrophobicity due to surface degradation caused by water impact.

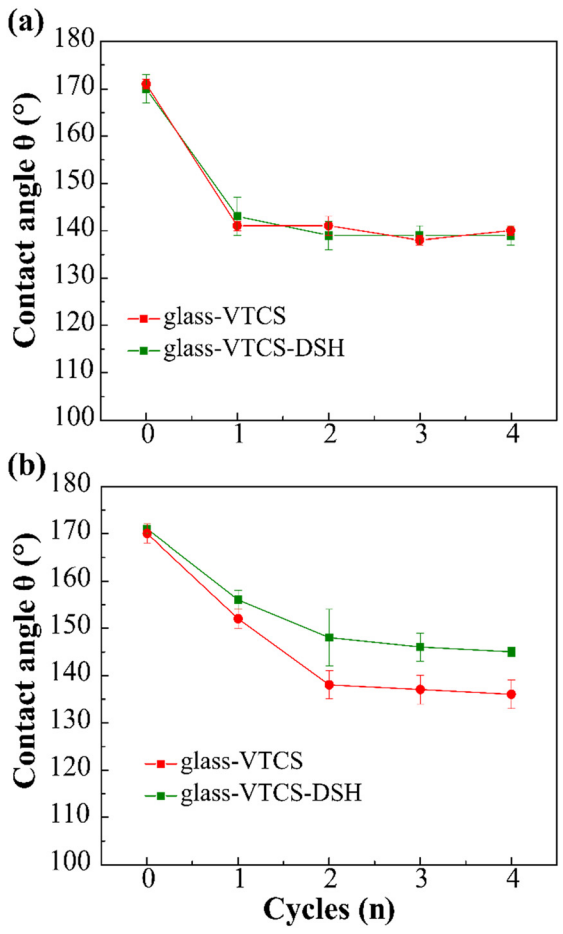

Fig. 7 Evolution of the water contact angle of the VTCS-modified glass samples before and after functionalization with DSH over multiple cycles under (a) a custom-designed waterfall impact test, and (b) a salt solution immersion test following ASTM B117.[100]

The salt solution immersion (Fig. 7b) highlighted the superior stability of the DSH-functionalized surfaces. The functionalized samples demonstrate higher resistance to degradation, maintaining their superhydrophobicity throughout the experiments. In contrast, the unfunctionalized samples exhibit a notable decrease in WCAs when subjected to chemical degradation. The salt immersion test revealed a gradual decline in hydrophobicity, with functionalized surfaces maintaining superhydrophobic properties to a minimum extent of ~150°.

The protocol for the thermal cycling test was designed based on the MQT11 thermal cycling test specified in IEC 61215-2.[101] Each cycle of this test involved exposing the sample to temperature variations ranging from −20 °C to 100 °C, with transitions at room temperature. The lower temperature limit (−20 °C) was achieved using a laboratory freezer (General UF 17CW1, USA), while the upper-temperature limit (100 °C) was attained using a laboratory oven (Fisher Scientific Isotemp 200 Series, USA). During transitions between extreme temperatures, samples were allowed to equilibrate to room temperature through heat exchange with the ambient environment on a bench. The thermal cycling profile (Fig. S6) followed these steps: cooling to −20 °C and holding for 2.5 h, equilibration to room temperature for 1 h, heating to 100 °C and holding for 2.5 h, and finally equilibration to room temperature. It should be noted that this protocol derives from the standard IEC 61215-2:2021[101] test conditions, which specify temperature extremes of −40 °C and 85 °C. Our modified approach accommodated our equipment limitations while subjecting the samples to significant thermal stress. While our thermal cycling protocol was conducted under ambient atmospheric condition, we acknowledge that performing such tests under inert and low-humidity environments may offer further insight into the stability of reactive surface groups such as vinyl. This remains an important direction for future work.

The thermal cycling test (Fig. 8) highlighted the superior stability of the functionalized surfaces. The functionalized samples demonstrate higher resistance to degradation, maintaining their superhydrophobicity throughout the experiments. In contrast, the unfunctionalized samples exhibit a notable decrease in WCAs when subjected to chemical and thermal degradation. The salt immersion test revealed a gradual decline in hydrophobicity, with functionalized surfaces maintaining superhydrophobic properties to a minimum extent ~150°. Similarly, the functionalized samples retained higher and more stable contact angles during thermal cycling, indicating enhanced thermal durability. These findings confirm the effectiveness of DSH functionalization in preserving the superhydrophobic properties under salt immersion and thermal cycling tests.

Open Access Article. Published on 02 September 2025. Downloaded on 2/12/2026 8:12:20 PM.
This article is licensed under a Creative Commons Attribution 3.0 Unported Licence.

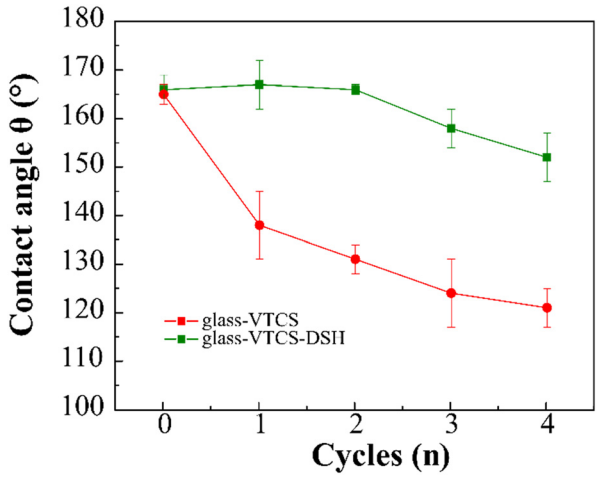

Fig. 8 Evolution of the water contact angle of the samples before and after functionalization over multiple cycles for thermal cycling test.

Conclusions

This study demonstrates that the initial molecular arrangement of VTCS and ATCS, prepared under the same reaction conditions, forming the coating structure on the glass surface, mainly determines the properties of the resulting coatings. VTCS developed a porous nanofilament network with superhydrophobic properties and enhanced transparency. In contrast, ATCS produced irregular aggregates with hydrophobic properties and enhanced transparency. Upon functionalization with DSH, the properties of the modified surfaces improved, preserving the initial coating structure with only slight modifications. For VTCS coating, functionalization increased superhydrophobicity from 168° ± 2 to 170° ± 4 and enhanced optical properties, increasing the transmittance by 4% compared to the pristine glass. The ATCS contact angles increased from 109° ± 4 to 113° ± 4 after functionalization, with a 2% increase in transmittance. Indeed, functionalized VTCS-modified surfaces demonstrated superior thermal and chemical stability, remaining superhydrophobic during the experiments. However, superhydrophobicity was not preserved during the water impact testing, as evidenced by a drop in WCA after the first cycle. Compared with VTCS, ATCS has an additional methylene group that increases its steric hindrance and flexibility, resulting in a heterogeneous coating with lower hydrophobicity. This structural difference led ATCS to form irregular aggregates. PiFM provided valuable insights into the spatial distribution of functionalization and reaction yield. From ATR-FTIR analysis, the thiol–ene click reaction conversion was estimated to be approximately 63% for VTCS- and 40% for ATCS-functionalized glass surfaces. Slightly lower conversions (56% for VTCS- and 33% for ATCS-) obtained by PiFM were attributed to variations in spatial resolution and sampling depth differences between the techniques. The lower yield for ATCS may be attributed to the inaccessibility of double bonds caused by the aggregate morphology. These findings highlight the importance of molecular structure in determining the coating properties and functionalization efficiency.

Author contributions

Conceptualization: CCHC, MS, AN. Data curation: NK, MJ, CCHC, AN. Formal analysis: NK, MJ, CCHC, AN. Funding acquisition: CCHC, MS, AN. Supervision: MS, AN. Resources: MS, AN. Writing – original draft: NK, AN. Writing – review & editing: NK, MJ, CCHC, MS, AN.

Conflicts of interest

The authors declare no conflict of interest.

Data availability

Supplementary information is available. See DOI: **https://doi.org/10.1039/D5LF00162E**.

The authors confirm that all data supporting the findings of this study are contained within the article and the SI.

Acknowledgements

This research was funded by MITACS, in collaboration with Edgehog Advanced Technologies Inc. We thank Professor Luc Stafford from Université de Montréal and NanoQAM for providing the equipment for the characterization of the glass surface coatings.

References

1 W. Barthlott and C. Neinhuis, *Planta*, 1997, **202**, 1–8.
2 W. Barthlott and N. Ehler, *Raster-elektronenmikroskopie der Epidermis-oberflächen von Spermatophyten*, Akademie der Wissenschaften und Literatur, Mainz, 1977.
3 C. Neinhuis and W. Barthlott, *Ann. Bot.*, 1997, **79**, 667–677.
4 T. Wagner, C. Neinhuis and W. Barthlott, *Acta Zool.*, 1996, **77**, 213–225.
5 J. P. Youngblood and N. R. Sottos, *MRS Bull.*, 2008, **33**, 732–741.
6 G. S. Watson, D. W. Green, L. Schwarzkopf, X. Li, B. W. Cribb, S. Myhra and J. A. Watson, *Acta Biomater.*, 2015, **21**, 109–122.
7 B. Su, Y. Tian and L. Jiang, *J. Am. Chem. Soc.*, 2016, **138**, 1727–1748.
8 M. Motamedi, M. E. Warkiani and R. A. Taylor, *Adv. Opt. Mater.*, 2018, **6**, 1800091.
9 H. Zhu, Y. Huang, X. Lou and F. Xia, *View*, 2021, **2**, 20200053.
10 M. Sun, G. S. Watson, Y. Zheng, J. A. Watson and A. Liang, *J. Exp. Biol.*, 2009, **212**, 3148–3155.
11 Y. Liu and G. Li, *J. Colloid Interface Sci.*, 2012, **388**, 235–242.
12 Z. Guo and W. Liu, *Plant Sci.*, 2007, **172**, 1103–1112.
13 L. Gao and T. J. McCarthy, *Langmuir*, 2006, **22**, 2966–2967.
14 S. Yu, Z. Guo and W. Liu, *Chem. Commun.*, 2015, **51**, 1775–1794.

© 2026 The Author(s). Published by the Royal Society of Chemistry

Open Access Article. Published on 02 September 2025. Downloaded on 2/12/2026 8:12:20 PM. This article is licensed under a Creative Commons Attribution 3.0 Unported Licence.

15 A. Y. Fadeev and T. J. McCarthy, *Langmuir*, 2000, **16**, 7268–7274.
16 J. J. Pesek and M. T. Matyska, *Interface Sci.*, 1997, **5**, 103–117.
17 T. Kondo, R. Yamada and K. Uosaki, in *Organized Organic Ultrathin Films*, ed. K. Ariga, Wiley-VCH, Weinheim, 2013, pp. 7–42.
18 S. R. Wasserman, Y. T. Tao and G. M. Whitesides, *Langmuir*, 1989, **5**, 1074–1087.
19 D. Nanda, P. Varshney, M. Satapathy, S. S. Mohapatra and A. Kumar, *Colloids Surf., A*, 2017, **529**, 231–238.
20 J. Zhang, L. Li, B. Li and S. Seeger, *RSC Adv.*, 2014, **4**, 33424–33430.
21 N. Jumrus, T. Chaisen, A. Sriboonruang, A. Panthawan, T. Kumpika, E. Kantarak, P. Singjai and W. Thongsuwan, *Mater. Lett.*, 2020, **264**, 127347.
22 G. Carson and S. Granick, *J. Appl. Polym. Sci.*, 1989, **37**, 2767–2772.
23 C. R. Kessel and S. Granick, *Langmuir*, 1991, **7**, 532–538.
24 D. K. Schwartz, S. Steinberg, J. Israelachvili and J. A. N. Zasadzinski, *Phys. Rev. Lett.*, 1992, **69**, 3354–3357.
25 J. Huang, X. Liu, X. Qiu, L. Xie, B. Yan, X. Wang, Q. Huang and H. Zeng, *J. Phys. Chem. B*, 2017, **121**, 3151–3161.
26 L. Gao and T. J. McCarthy, *J. Am. Chem. Soc.*, 2006, **128**, 9052–9053.
27 H. S. Khoo and F. G. Tseng, *Nanotechnology*, 2008, **19**, 345603.
28 W. Noll, *Chemistry and technology of silicones*, Elsevier, Amsterdam, 2012.
29 M. E. McGovern, K. M. R. Kallury and M. Thompson, *Langmuir*, 1994, **10**, 3607–3614.
30 S. Sriram, R. K. Singh and A. Kumar, *Surf. Interfaces*, 2020, **19**, 100472.
31 A. Matin, U. Baig, S. Akhtar, N. Merah, M. A. Gondal, A. H. Bake and A. Ibrahim, *Prog. Org. Coat.*, 2019, **136**, 105192.
32 R. Banga, J. Yarwood, A. M. Morgan, B. Evans and J. Kells, *Langmuir*, 1995, **11**, 4393–4399.
33 A. Stojanovic, G. R. J. Artus and S. Seeger, *Nano Res.*, 2010, **3**, 889–894.
34 D. Zahner, J. Abagat, F. Svec, J. M. J. Fréchet and P. A. Levkin, *Adv. Mater.*, 2011, **23**, 3030–3034.
35 Y. J. Kim, K. H. Lee, H. Sano, J. Han, T. Ichii, K. Murase and H. Sugimura, *Jpn. J. Appl. Phys.*, 2008, **47**, 307.
36 B. Indumathy, P. Sathiyanathan, G. Prasad, M. S. Reza, A. A. Prabu and H. I. Kim, *Polymer*, 2023, **15**, 2517.
37 D. Zhang, J. Ji, C. Yan, J. Zhang, Z. An and Y. Shen, *Ind. Eng. Chem.*, 2024, **140**, 20–46.
38 K. Suzuki, L. Malfatti, M. Takahashi, D. Carboni, F. Messina, Y. Tokudome, M. Takemoto and P. Innocenzi, *Sci. Rep.*, 2017, **7**, 5469.
39 Z. Li, C. Song, Q. Li, X. Xiang, H. Yang, X. Wang and J. Gao, *Coatings*, 2019, **9**, 453.
40 K. S. Lee and R. J. Ram, *Lab Chip*, 2009, **9**, 1618–1624.
41 Y. C. Chen, K. Li, S. Zhang, L. Qin, S. Deng, L. Ge, L. P. Xu, L. Ma, S. Wang and X. Zhang, *ACS Nano*, 2020, **14**, 4654–4661.
42 M. Y. Moskalik and B. A. Shainyan, *Russ. Chem. Rev.*, 2024, **93**, 1–34.
43 J. Li, L. Li, X. Du, W. Feng, A. Welle, O. Trapp, M. Grunze, M. Hirtz and P. A. Levkin, *Nano Lett.*, 2015, **15**, 675–681.
44 A. Babik, J. Mistrik, J. Zemek and V. Cech, *J. Adhes. Sci. Technol.*, 2012, **26**, 2543–2554.
45 A. Menawat, H. Joseph and R. Siriwardane, *J. Colloid Interface Sci.*, 1984, **101**, 110–119.
46 J. X. H. Wong and H. Z. Yu, *J. Chem. Educ.*, 2013, **90**, 1203–1206.
47 X. Guo-hua and K. Higashitani, *J. Zhejiang Univ., Sci., A*, 2000, **1**, 162–170.
48 M. Jin, J. Wang, X. Yao, M. Liao, Y. Zhao and L. Jiang, *Adv. Mater.*, 2011, **23**, 2861–2864.
49 G. R. J. Artus, S. Jung, J. Zimmermann, H.-P. Gautschi, K. Marquardt and S. Seeger, *Adv. Mater.*, 2006, **18**, 2758–2762.
50 H. J. Jeong, D. K. Kim, S. B. Lee, S. H. Kwon and K. Kadono, *J. Colloid Interface Sci.*, 2001, **235**, 130–134.
51 P. W. Erickson, *J. Adhes.*, 1970, **2**, 131–146.
52 S. P. Pujari, L. Scheres, A. T. M. Marcelis and H. Zuilhof, *Angew. Chem., Int. Ed.*, 2014, **53**, 6322–6356.
53 T. F. E. Materne, F. d. Buyl and G. L. Witucki, *Organosilane Technology in Coating Applications: Review and Perspectives*, Dow Corning Corporation, Midland, 2012.
54 M. Novotný and K. D. Bartle, *Chromatographia*, 1970, **3**, 272–274.
55 S. Cheawchan, S. Uchida, H. Sogawa, Y. Koyama and T. Takata, *Langmuir*, 2016, **32**, 309–315.
56 N. Khitas, C. C. H. Cheng and A. Nazemi, *Can. J. Chem.*, 2025, **103**, 174–183.
57 M. Vista, Scientific Principles of PiFM and PiF-IR, **https://molecularvista.com/technology/pifm-and-pif-ir/scientific-principles/**, (accessed March 26, 2025).
58 J. Li and J. H. Horton, *J. Mater. Chem.*, 2002, **12**, 1268–1273.
59 D. A. E. Rollings and J. G. C. Veinot, *Langmuir*, 2008, **24**, 13653–13662.
60 R. Harrop, *Surf. Technol.*, 1978, **6**, 385–393.
61 S. Shen, G. A. Guirgis and J. R. Durig, *Struct. Chem.*, 2001, **12**, 33–43.
62 D. Zarubin, *Phys. Chem. Glasses*, 1999, **40**, 184–192.
63 S.-i. Amma, S. H. Kim and C. G. Pantano, *J. Am. Ceram. Soc.*, 2016, **99**, 128–134.
64 E. R. Shull, R. A. Thursack and C. M. Birdsall, *J. Chem. Phys.*, 1956, **24**, 147–150.
65 J. R. Durig and K. L. Hellams, *Appl. Spectrosc.*, 1968, **22**, 153–160.
66 R. E. Scott and K. C. Frisch, *J. Am. Chem. Soc.*, 1951, **73**, 2599–2600.
67 A. L. Smith, *Spectrochim. Acta*, 1960, **16**, 87–105.
68 G. A. Guirgis, Y. E. Nashed, T. K. Gounev and J. R. Durig, *Struct. Chem.*, 1998, **9**, 265–277.
69 D. L. Bailey and A. N. Pines, *Ind. Eng. Chem.*, 1954, **46**, 2363–2367.
70 Y. S. Li, N. E. Vecchio, Y. Wang and C. McNutt, *Spectrochim. Acta, Part A*, 2007, **67**, 598–603.

Open Access Article. Published on 02 September 2025. Downloaded on 2/12/2026 8:12:20 PM.
This article is licensed under a Creative Commons Attribution 3.0 Unported Licence.

71 D. A. E. Rollings, S. Tsoi, J. C. Sit and J. G. C. Veinot, *Langmuir*, 2007, **23**, 5275–5278.
72 A. Nakajima, K. Hashimoto, T. Watanabe, K. Takai, G. Yamauchi and A. Fujishima, *Langmuir*, 2000, **16**, 7044–7047.
73 S. J. Choi and S. Y. Huh, *Macromol. Rapid Commun.*, 2010, **31**, 539–544.
74 R. G. Karunakaran, C. H. Lu, Z. Zhang and S. P. Yang, *Langmuir*, 2011, **27**, 4594–4602.
75 J. X. H. Wong, H. Asanuma and H. Z. Yu, *Thin Solid Films*, 2012, **522**, 159–163.
76 A. Nakajima, *J. Ceram. Soc. Jpn.*, 2004, **112**, 533–540.
77 A. Nakajima, A. Fujishima, K. Hashimoto and T. Watanabe, *Adv. Mater.*, 1999, **11**, 1365–1368.
78 J. Zhang and S. Seeger, *ChemPhysChem*, 2013, **14**, 1646–1651.
79 J. Zimmermann, A. G. R. J. Artus and S. Seeger, *J. Adhes. Sci. Technol.*, 2008, **22**, 251–263.
80 S. L. Diedenhofen, G. Vecchi, R. E. Algra, A. Hartsuiker, O. L. Muskens, G. Immink, E. P. A. M. Bakkers, W. L. Vos and J. G. Rivas, *Adv. Mater.*, 2009, **21**, 973–978.
81 V. H. Dalvi and P. J. Rossky, *Proc. Natl. Acad. Sci. U. S. A.*, 2010, **107**, 13603–13607.
82 L. Liang, T. Wen, J. Xin, C. Su, K. Song, W. Zhao, H. Liu and G. Su, *Molecules*, 2023, **28**, 905.
83 F. Arianpour, M. Farzaneh and R. Jafari, *Prog. Org. Coat.*, 2016, **93**, 41–45.
84 J. Bravo, L. Zhai, Z. Wu, R. E. Cohen and M. F. Rubner, *Langmuir*, 2007, **23**, 7293–7298.
85 Y. Rahmawan, L. Xu and S. Yang, *J. Mater. Chem. A*, 2013, **1**, 2955–2969.
86 H. Heywood, *J. Soc. Chem. Ind.*, 1937, **56**, 149–154.
87 J. A. Davies-Jones and P. R. Davies, *J. Soc. Chem. Ind., London*, 2022, **6**, 1552–1573.
88 A. Amini, P. Tirgar, A. Bahmani, M. Jafari, M. Siaj, F. Barthelat and A. Ehrlicher, *Adv. Funct. Mater.*, 2024, **34**, 2405008.
89 M. Jafari, S. Salek, G. Goubert, J. C. Byers and M. Siaj, *J. Phys. Chem. C*, 2024, **128**, 21720–21729.
90 J. Sagiv, *J. Am. Chem. Soc.*, 1980, **102**, 92–98.
91 M. J. Stevens, *Langmuir*, 1999, **15**, 2773–2778.
92 S. Grigoras and T. H. Lane, *J. Comput. Chem.*, 1988, **9**, 25–39.
93 A. K. Tucker-Schwartz, R. A. Farrell and R. L. Garrell, *J. Am. Chem. Soc.*, 2011, **133**, 11026–11029.
94 M. Kaczmarek, A. Przybylska, A. Szymańska, A. Dutkiewicz and H. Maciejewski, *Sci. Rep.*, 2023, **13**, 21025.
95 M. A. C. Campos, J. M. J. Paulusse and H. Zuilhof, *Chem. Commun.*, 2010, **46**, 5512–5514.
96 Y. Zhang, C. W. Chu, W. Ma and A. Takahara, *ACS Omega*, 2020, **5**, 7488–7496.
97 C. I. Biggs, M. Walker and M. I. Gibson, *Biomacromolecules*, 2016, **17**, 2626–2633.
98 G. B. Darband, M. Aliofkhazraei, S. Khorsand, S. Sokhanvar and A. Kaboli, *Arabian J. Chem.*, 2020, **13**, 1763–1802.
99 I. Malavasi, I. Bernagozzi, C. Antonini and M. Marengo, *Surf. Innovations*, 2015, **3**, 49–60.
100 *Standard Practice for Operating Salt Spray (Fog) Apparatus*, Report ASTM B117-16, ASTM International, 2016.
101 *Terrestrial Photovoltaic (PV) Modules – Design Qualification and Type Approval – Part 2: Test Procedures*, Report IEC 61215-2, International Electrotechnical Commission, 2021.
102 C. Xuan, S. Xiaoran, S. Zhaoji, Z. Jiaen, Q. Zhong, X. Huimin and W. Hui, *J. Resour. Ecol.*, 2021, **12**(593–599), 597.
103 A. B. D. Cassie and S. Baxter, *Trans. Faraday Soc.*, 1944, **40**, 546–551.
104 A. B. D. Cassie, *Discuss. Faraday Soc.*, 1948, **3**, 11–16.
105 P. Papadopoulos, L. Mammen, X. Deng, D. Vollmer and H. J. Butt, *Proc. Natl. Acad. Sci. U. S. A.*, 2013, **110**, 3254–3258.

© 2026 The Author(s). Published by the Royal Society of Chemistry